

Blue straggler stars beyond the Milky Way. III. Detection of evolved blue straggler candidates in Large Magellanic Cloud clusters

CHENGYUAN LI,¹ LICAI DENG,² KENJI BEKKI,³ JONGSUK HONG,⁴ RICHARD DE GRIJS,^{1,5,4} AND BI-QING FOR^{3,6}

¹*Department of Physics and Astronomy, Macquarie University, Sydney, NSW 2109, Australia*

²*Key Laboratory for Optical Astronomy, National Astronomical Observatories, Chinese Academy of Sciences, 20A Datun Road*

³*International Centre for Radio Astronomy Research/The University of Western Australia, M468, 35 Stirling Highway, Crawley, WA6009, Australia*

⁴*Kavli Institute for Astronomy and Astrophysics, Peking University, Yi He Yuan Lu 5, Hai Dian District, Beijing 100871, China*

⁵*International Space Science Institute-Beijing, 1 Nanertiao, Zhongguancun, Hai Dian District, Beijing 100190, China*

⁶*Australian Research Council, Centre of Excellence for All-sky Astrophysics in 3 Dimensions*

Submitted to AJ

ABSTRACT

We analyze *Hubble Space Telescope* observations of nine Large Magellanic Cloud star clusters with ages of 1–2 Gyr to search for evolved counterparts of blue straggler stars. Near the red clump regions in the clusters' color–magnitude diagrams, we find branches of evolved stars that are much brighter than normal evolved stars. We examine the effects of photometric artifacts, differential reddening, and field contamination. We conclude that these bright evolved stars cannot be explained by any of these effects. Our statistical tests show that the contributions of photometric uncertainties and crowding effects, as well as that owing to differential reddening, to these bright evolved stars are insufficient to fully explain the presence of these bright evolved stars. Based on isochrone fitting, we also ruled out the possibility that these bright evolved stars could be reproduced by an internal chemical abundance spread. The spatial distributions of the bright evolved stars exhibit clear concentrations that cannot be explained by homogeneously distributed field stars. This is further confirmed based on Monte Carlo-based tests. By comparing our observations with stellar evolution models, we find that the masses of most of bright evolved stars do not exceed twice the average mass of normal evolved stars. We suggest that these bright evolved stars are, in fact, evolved blue straggler stars.

Keywords: blue stragglers — galaxies: star clusters — Hertzsprung-Russell and C-M diagrams — Magellanic Clouds

1. INTRODUCTION

Blue straggler stars (BSSs), which are commonly found in dense stellar systems like globular clusters (GCs) or open clusters (OPs), are stars located along the blue extension of the main-sequence turnoff (MSTO) regions in the color–magnitude diagrams (CMDs) of star clusters. It is thought that they are main-sequence (MS)-like stars that are significantly more massive than the cluster's bulk population (e.g., Ferraro et al. 2012; Baldwin et al. 2016; Raso et al. 2017). They represent a population of rejuvenated stars formed through dy-

namical evolution of old population stars. Since the host clusters have already exhausted all of their gas, BSSs are unlikely traditional star-forming products, presumed to have resulted from the collapse of a molecular cloud. Two leading mechanisms invoked to retain BSSs on the MS include binary mass transfer and the eventual merger of both binary components (Andronov et al. 2006; Hills & Day 1976), and direct stellar collisions (McCrea 1964).

The evolved counterparts of most BSSs (eBSSs) in old GCs are photometrically indistinguishable from normal stars undergoing advanced stages of stellar evolution. The best locus to search for eBSSs in old OCs is the horizontal branch (HB), where stars are placed according to their mass. Using this approach, Ferraro et al.

(1997) detected 19 eBSSs in the core region of the GC M3. Possible eBSSs can also be identified by studying the number of stars in the asymptotic giant branch (AGB) region. Beccari et al. (2006) found a significant excess of AGB stars in the GC 47 Tuc. They interpreted this pattern as a result of the progeny of massive stars originating from the evolution of binary systems. Using stellar spectra and chemical abundances, Ferraro et al. (2016) identified an eBSSs mass that is significantly higher than the MSTO mass in the GC 47 Tuc.

In old stellar populations like those found in most GCs, stars that have evolved into red giants now supported by helium fusion in their cores will develop a red clump (RC) in the CMD. The RC properties are independent of their internal age spread, and thus they end up with the same luminosity. For younger stellar populations ($\lesssim 2$ Gyr), such as those dominating young massive clusters (YMCs) or OCs, the magnitude extent of the RCs is a function of age. Inclusion of an evolved blue straggler population will contribute to the extension of the RC, thus making eBSSs distinguishable from normal RC stars. Studying younger star clusters is therefore a promising way to photometrically search for eBSSs. However, almost all young Galactic clusters are located in the Galactic disk. They are affected by severe foreground extinction, which will elongate the RCs in the CMDs, thus masking the difference between eBSSs and normal RC stars. Star clusters in the Large Magellanic Cloud (LMC) cover a much more extended age range than those in the Milky Way (MW). In addition, the LMC is located at high Galactic latitude, where Galactic extinction is small. LMC clusters are therefore ideal targets to search for eBSSs in younger star clusters.

Only few studies have explored BSSs in Magellanic Cloud star clusters. Li et al. (2013) examined 162 BSSs in the old LMC GC Hodge 11. They found that its blue straggler population is split into two clumps characterized by different colors. Those in the cluster’s central region are systematically bluer than their counterparts further out. Li et al. (2018) found two distinct BSS populations in a young (1–2 Gyr-old) LMC GC, NGC 2173, a situation that is similar to those found in GGCs (e.g., Ferraro et al. 2009; Dalessandro et al. 2013; Simunovic et al. 2014). However, unlike GGCs exhibiting bifurcated BSS populations, no evidence of any putative post-core-collapse event was detected in this cluster. Li & Hong (2018) analyzed the BSSs in the young LMC GC NGC 2213. They found that although this cluster’s population of BSSs has a half-mass relaxation time that is shorter than the cluster’s isochronal age, the BSSs in NGC 2213 are not fully segregated. They suggest that this is likely caused by interactions between the BSSs’

progenitor binaries and black hole subsystems, as well as by dynamical disruption of binaries in this young GC. Sun et al. (2018) studied BSSs in 24 Magellanic Cloud clusters. They derived a sub-linear correlation between the number of BSSs in the cluster cores and the clusters’ core masses. They concluded that this may be an indication of a binary origin for these BSSs, which is consistent with similar conclusions regarding BSSs in Milky Way GCs (Knigge et al. 2009).

In this paper, we search for eBSSs in nine LMC young GCs. We find that all of these clusters harbor samples of evolved stars that are located in the bright extension of their RCs. We rule out the possibilities that these bright evolved stars are simply caused by photometric artifacts (such as crowding) and measurement uncertainties, by differential reddening, by field-star contamination, or by an internal chemical abundance spread. For almost all these bright evolved stars, their masses do not exceed twice the average mass of normal stars if we assume that they are all single stellar systems. We suggest that the most straightforward interpretation of our observations is that they are eBSSs.

This article is organized as follows. In Section 2 we introduce the details of our observations and the data reduction. Section 3 presents our main results. In Section 4 we provide a brief physical discussion about the origins of these bright evolved stars. Section 5 contains a summary.

2. OBSERVATIONS AND DATA REDUCTION

All clusters studied in this work were observed with the *HST*’s Ultraviolet and Visible channel of the Wide Field Camera 3 (UVIS/WFC3) or with the Wide Field Channel of the Advanced Camera for Surveys (ACS/WFC). For each cluster, except for NGC 1644, we also adopted a parallel observation of a nearby region as reference field, which will be used to statistically estimate the level of field-star contamination. For NGC 1644 we did not find a proper parallel observation that can represent its reference field, but we will show that the edge of the science image that includes the main cluster is sufficient to represent a reference field. Relevant information pertaining to the data set is present in Table 1.

For each cluster, we performed point-spread-function (PSF) photometry on the flat-fielded frames (`'_flt'`) of the science images using the WFC3 and ACS modules implemented in the DOLPHOT 2.0 package¹. To compile the resulting stellar catalog, we adopted a filter employing the sharpness and ‘crowding’ parameters calculated

¹ <http://americano.dolphinim.com>

Table 1. Description of the science images used in this article.

Cluster	Camera	Exposure time	Filter	Program ID	PI name
NGC 1644*	ACS/WFC	250 s 170 s	F555W F814W	GO-9891	G. Gilmore
NGC 1651 (Cluster)	UVIS/WFC3	120 s+600 s+720 s 30 s + 2×700 s	F475W F814W	GO-12257	L. Girardi
NGC 1651 (Ref. Field)	ACS/WFC	2×500 s 2×500 s	F475W F814W	GO-12257	L. Girardi
NGC 1783 (Cluster)	ACS/WFC	40 s + 2×340 s 8 s + 2×340 s	F555W F814W	GO-10595	P. Goudfrooij
NGC 1783 (Ref. Field)	ACS/WFC	2×350 s 80 s + 300 s + 340 s	F555W F814W	GO-12257	L. Girardi
NGC 1806 (Cluster)	ACS/WFC	40 s + 2×340 s 8 s + 2×340 s	F555W F814W	GO-10595	P. Goudfrooij
NGC 1806 (Ref. Field)	ACS/WFC	2×350 s 80 s + 300 s + 340 s	F555W F814W	GO-12257	L. Girardi
NGC 1846 (Cluster)	ACS/WFC	40 s + 2×340 s 8 s + 2×340 s	F555W F814W	GO-10595	P. Goudfrooij
NGC 1846 (Ref. Field)	UVIS/WFC3	2×348 s 2×400 s	F555W F814W	GO-12326	N. Keith
NGC 1852 (Cluster)	ACS/WFC	330 s 200 s	F555W F814W	GO-9891	G. Gilmore
NGC 1852 (Ref. Field)	ACS/WFC	2×500 s 2×350 s	F555W F814W	GO-12257	L. Girardi
NGC 2154 (Cluster)	ACS/WFC	300 s 200 s	F555W F814W	GO-9891	G. Gilmore
NGC 2154 (Ref. Field)	ACS/WFC	2×500 s 2×350 s	F555W F814W	GO-12257	L. Girardi
NGC 2203 (Cluster)	UVIS/WFC3	120 s+2×700 s 30 s + 2×700 s	F475W F814W	GO-12257	L. Girardi
NGC 2203 (Ref. Field)	ACS/WFC	90 s + 2×500 s + 2×700 s 10 s + 550 s + 690 s + 2×713 s	F475W F814W	GO-12257	L. Girardi
NGC 2213 (Cluster)	UVIS/WFC3	120 s+600 s+720 s 30 s + 2×700 s	F475W F814W	GO-12257	L. Girardi
NGC 2213 (Ref. Field)	ACS/WFC	2×500 s 2×500 s	F475W F814W	GO-12257	L. Girardi

*: includes both the cluster region and the reference field.

by DOLPHOT2.0. The sharpness illustrates the broadness of a detected object relative to the PSF. A perfect star should have a zero sharpness. A negative sharpness may indicate an object that is too sharp (like a cosmic ray), while a very large positive value means that the detected object is too broad (for example, a background galaxy). The crowding quantifies how much brighter an object would have been measured had nearby stars not been fitted simultaneously (in units of magnitudes). An isolated star would have zero crowding. We selected only objects with $-0.3 \leq \text{sharpness} \leq 0.3$ and $\text{crowding} \leq 0.5$ mag in all frames used for our analysis. We only kept ob-

jects classified as good stars, and not centrally saturated, by DOLPHOT2.0. DOLPHOT2.0 also automatically combined stellar catalog resulting from frames with different exposure times into a deep catalog, eventually resulting in a deep, multi-band stellar catalog. In this paper, we only focus on evolved stars. These stars are bright and usually have good photometric quality. We confirmed that performing our data reduction only has a minor effect on the stars of interest: fewer than 5% would be removed by the data reduction procedures adopted.

For all clusters, except NGC 1644, we have access to two parallel observations, which represent the star clus-

ter region and its nearby reference field. This information is also included in Table 1. For NGC 1644, we simply adopted the peripheral region in the same image, for distances to the cluster center greater than 20 pc, as reference field. As we will show below, the best-fitting tidal radius to the brightness profile of NGC 1644 is less than 20 pc. Our adoption of a ‘field’ region in the same image that contains the cluster itself is therefore reasonable. All other clusters, except NGC 1783, have parallel observations of reference fields located close to or well beyond the clusters’ tidal radii. NGC 1783 is so large that even a parallel observation centered ~ 100 pc from the cluster center does not reach its tidal radius. However, the *HST* archive² does not contain any observations beyond the cluster’s tidal radius obtained through the same passbands. The adopted reference field for NGC 1783 is therefore a compromise. As we will show, although we have adopted a reference field that is actually located too close to the cluster, field contamination in the region of interest is minor.

Our cluster CMDs are presented in Fig. 1.

Before we search for eBSS candidates in our sample clusters, we first calculated their brightness profiles, which will allow us to derive the clusters’ structural parameters (e.g. core, half-light, and tidal radii). To obtain reliable structural parameters, we first calculated the clusters’ center coordinates. After transferring the CCD coordinates (X, Y) to equatorial coordinates ($\alpha_{J2000}, \delta_{J2000}$) for all detected stars, we calculated the stellar number density contours for each cluster. We then defined the position where the stellar number density reaches its maximum value as the cluster center. For each cluster, we selected all stars brighter than a given magnitude in the F814W filter as a subsample. This magnitude limit is about two or three magnitudes brighter than the detection limit. We then used this subsample to study the clusters’ brightness profiles. We only selected these bright sample stars because (1) these stars will have a high completeness level and (2) in a stellar system, massive stars contribute most of the flux.

We used the cluster center to define different annular rings. This approach was applied to the observations of both the cluster image and the reference field. We adopted radial intervals between each pair of successive annular rings of 1 pc. For each ring, we calculated the total flux of stars (in the F814W filter), $f(r) = \sum 10^{(F814W - (m - M)_0 / (-2.5))}$. The flux density is $\rho(r) = f(r)/A(r)$, corresponding to a surface brightness of $\mu(r) = -2.5 \log \rho(r) + (m - M)_0$. In principle, the to-

tal flux in each ring should contain the contributions of both cluster as well as field stars. This brightness profile can be described by a King model combined with a constant (representing the field brightness), (King 1962).

$$\mu(r) = k \left[\frac{1}{\sqrt{1 + (r/r_c)^2}} - \frac{1}{\sqrt{1 + (r_t/r_c)^2}} \right] + b. \quad (1)$$

Here, r_c and r_t are the core and tidal radii, respectively; b is a constant which represents the background level, and k is a normalization coefficient. The derived brightness profiles for our clusters, as well as their best-fitting King models, are presented in Fig. 2. We have assumed that the uncertainties in the brightness are Poisson-like.

We calculated the clusters’ half-light radii, r_{hl} , based on their best-fitting King models. The derived center coordinates for our clusters, as well as their best-fitting structural parameters (r_c , r_{hl} , and r_t), are presented in Table 2.

Here we see that, except for NGC 1644, all clusters have tidal radii of at least ~ 30 pc. For comparison, the field of view (FOV) of ACS/WFC is $202'' \times 202''$; at the distance of the LMC, this is equal to a square with an area of $\sim 48.5 \times 48.5$ pc². The clusters NGC 1651, NGC 1718, NGC 2203, and NGC 2213 were observed with the UVIS/WFC3. Its FOV is even smaller, $162'' \times 162''$ ($\sim 38.9 \times 38.9$ pc²). The tidal radius derived for NGC 1644 is only ~ 20 pc, so that adopting the edge of the image as reference field is therefore reasonable. For the other clusters, we use the parallel observations as their reference fields. In Table 2, we also list the median distances of stars in the reference fields to the cluster centers. Because of the large sizes of our clusters, in Fig. 1, most CMDs contain stars from across the full cluster images. For NGC 1644, however, the CMD of the cluster region contains only stars within 20 pc from the cluster center.

3. MAIN RESULTS

In Fig. 3 we present the CMDs of our nine clusters, zoom into the regions centered on their RCs. All clusters contain a sample of stars located to the bright and blue side of the RC and the AGB. These stars are likely evolved stars, although they are more massive than normal giant stars. To select these stars we first use the PARSEC isochrones to fit our observations based on visual inspection (Bressan et al. 2012). For each cluster, we use an isochrone with a older age to fit the bulk stellar population, while we use two younger isochrones to roughly describe the bottom and top boundaries of the sample of bright evolved stars. The bottom boundary is the isochrone that crosses the bluer and brighter side of the RC in the cluster of interest, chosen to avoid

² <https://archive.stsci.edu/hst/search.php>

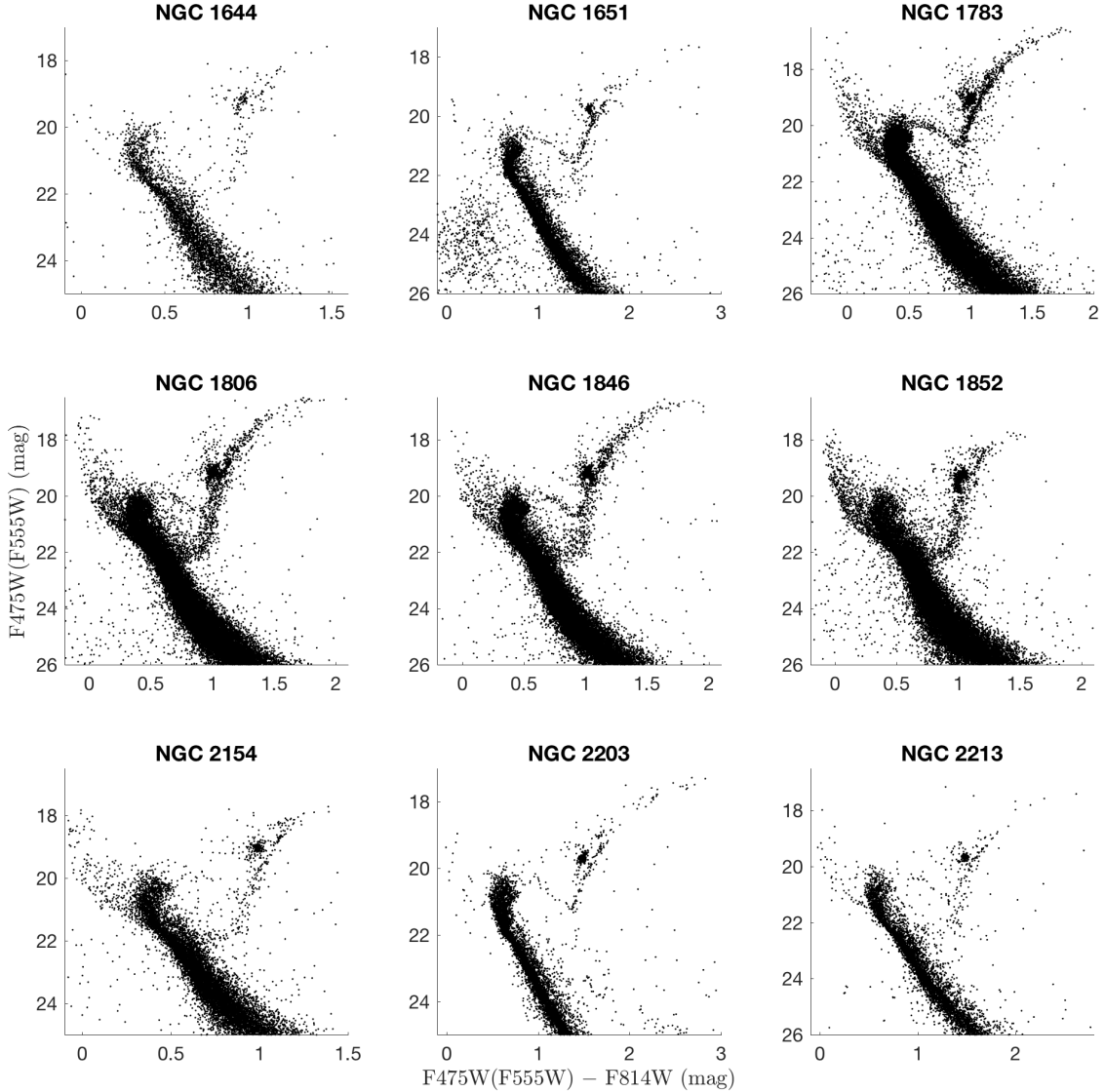


Figure 1. Processed CMDs for all clusters studied in this paper.

selecting too many stars that are affected by photometric scatter. These bottom boundaries should go across the region where the stellar number density is significantly lower than that in the RC. For the top boundary, we tried different isochrones pertaining to a range of younger ages to fit these bright evolved stars. We chose the isochrone that best covered most of the brightest stars in our sample clusters as the top boundary. Stars used to determine the top boundaries are indicated by arrows in Fig. 3. The adopted parameters are presented in Table 3. Our best-fitting parameters are close to or

consistent with those of Milone et al. (2009); Li et al. (2014); Niederhofer et al. (2016).

For each cluster, we first adopted stars that are redder than the middle point of the subgiant branch (SGB) as our sample stars, based on the adopted two young isochrones. Stars that are covered by the top and bottom boundaries are identified as bright evolved stars and will be used for analysis. In Fig. 3, the selected bright evolved stars are highlighted by dark blue circles. For each cluster, the same selection method was also applied to the CMDs of their reference fields. The field contaminants are highlighted by light blue squares.

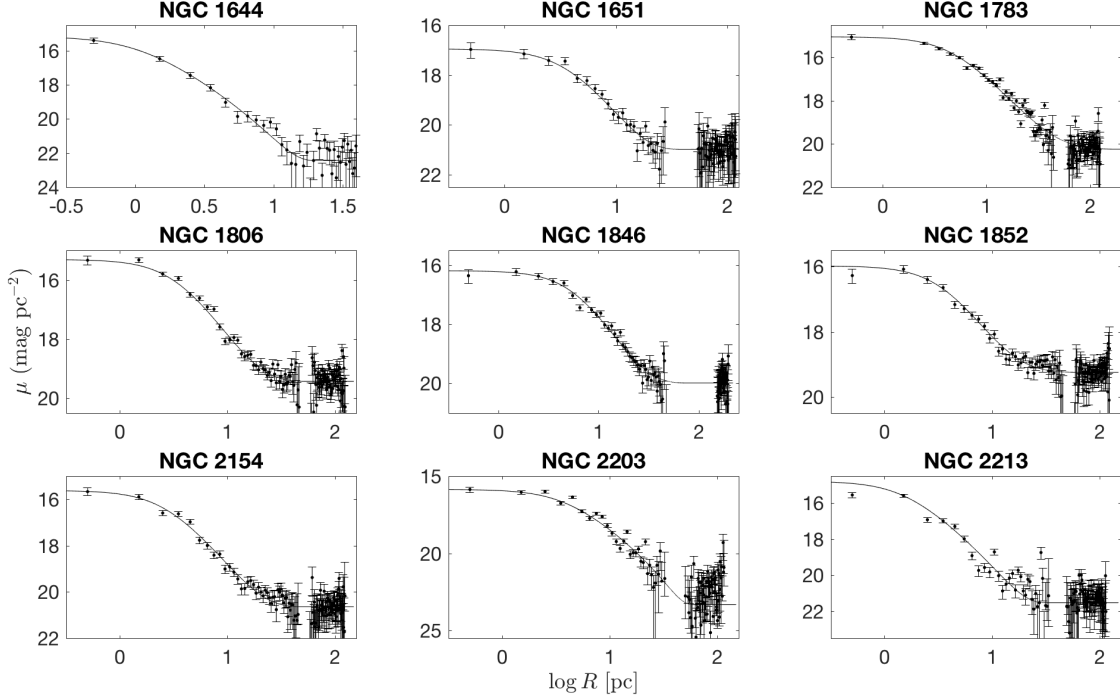


Figure 2. Brightness profiles (in the F814W filter) of our sample clusters. The solid curves represent the best-fitting King models.

Table 2. Derived structural parameters. Second to sixth columns: center right ascension and declination, core, half-light, and tidal radii, and median distance to the cluster center for the reference field stars.

Cluster	α_{J2000}^* (deg)	δ_{J2000}^* (deg)	r_c (pc)	r_{hl}^{\S} (pc)	r_t (pc)	\tilde{r}_f^{\dagger} (pc)
NGC 1644	$04^{\text{h}}37^{\text{m}}39.84^{\text{s}} \pm 0.48^{\text{s}}$	$-66^{\circ}11'56.40'' \pm 3.60''$	1.04 ± 0.01	$2.34^{+0.16}_{-0.74}$	19.57 ± 0.52	28.10
NGC 1651	$04^{\text{h}}37^{\text{m}}31.80^{\text{s}} \pm 0.48^{\text{s}}$	$-70^{\circ}35'07.08'' \pm 3.60''$	3.59 ± 0.11	$5.86^{+0.64}_{-0.36}$	36.64 ± 4.91	88.32
NGC 1783	$04^{\text{h}}59^{\text{m}}08.88^{\text{s}} \pm 0.60^{\text{s}}$	$-65^{\circ}59'13.20'' \pm 3.60''$	4.68 ± 0.13	$13.82^{+0.68}_{-0.32}$	181.20 ± 115.17	95.95
NGC 1806	$05^{\text{h}}02^{\text{m}}12.12^{\text{s}} \pm 0.60^{\text{s}}$	$-67^{\circ}59'07.80'' \pm 3.60''$	3.39 ± 0.09	$6.98^{+0.52}_{-0.48}$	52.60 ± 10.35	94.22
NGC 1846	$05^{\text{h}}07^{\text{m}}34.68^{\text{s}} \pm 0.48^{\text{s}}$	$-67^{\circ}27'32.40'' \pm 3.60''$	5.81 ± 0.11	$10.72^{+0.78}_{-0.22}$	73.84 ± 8.08	175.59
NGC 1852	$05^{\text{h}}09^{\text{m}}23.76^{\text{s}} \pm 0.36^{\text{s}}$	$-67^{\circ}46'48.00'' \pm 3.60''$	3.64 ± 0.07	$7.57^{+0.93}_{-0.07}$	61.11 ± 8.88	93.31
NGC 2154	$05^{\text{h}}57^{\text{m}}38.16^{\text{s}} \pm 0.36^{\text{s}}$	$-67^{\circ}15'46.80'' \pm 3.60''$	2.61 ± 0.08	$5.72^{+0.78}_{-0.22}$	48.00 ± 12.31	92.61
NGC 2203	$06^{\text{h}}10^{\text{m}}42.24^{\text{s}} \pm 0.36^{\text{s}}$	$-71^{\circ}31'44.76'' \pm 3.60''$	3.62 ± 0.08	$7.51^{+0.99}_{-0.01}$	59.33 ± 10.44	84.58
NGC 2213	$06^{\text{h}}10^{\text{m}}42.24^{\text{s}} \pm 0.48^{\text{s}}$	$-71^{\circ}31'44.76'' \pm 3.60''$	1.48 ± 0.04	$3.53^{+0.97}_{-0.03}$	31.31 ± 2.18	84.05

*: The uncertainty is equal to the size of the spatial bins adopted to calculate the number density contours.

§: The uncertainty is set equal to the radial interval (1 pc between two radial bins).

†: Median distance to the cluster center for all stars in the reference field.

However, except for NGC 1644, we cannot directly compare the observed bright evolved stars with their counterparts in the reference fields. This is because the observed fields usually have different exposure times than the cluster regions. Completeness levels in the same part of the CMDs between the reference field and the cluster are therefore usually different. For most of our clusters, the reference field observations do not include images with short exposure times. Bright evolved

stars observed in the cluster region may be saturated in the reference field. In such cases, we may not be able to quantify how many field stars could contaminate this very bright CMD region. Therefore, we removed some bright evolved stars from the cluster sample so as to conduct a fair comparison. We generated a sample of artificial stars with same magnitudes as our selected bright evolved stars. We then added all of these artificial candidates to the reference field and recovered them using

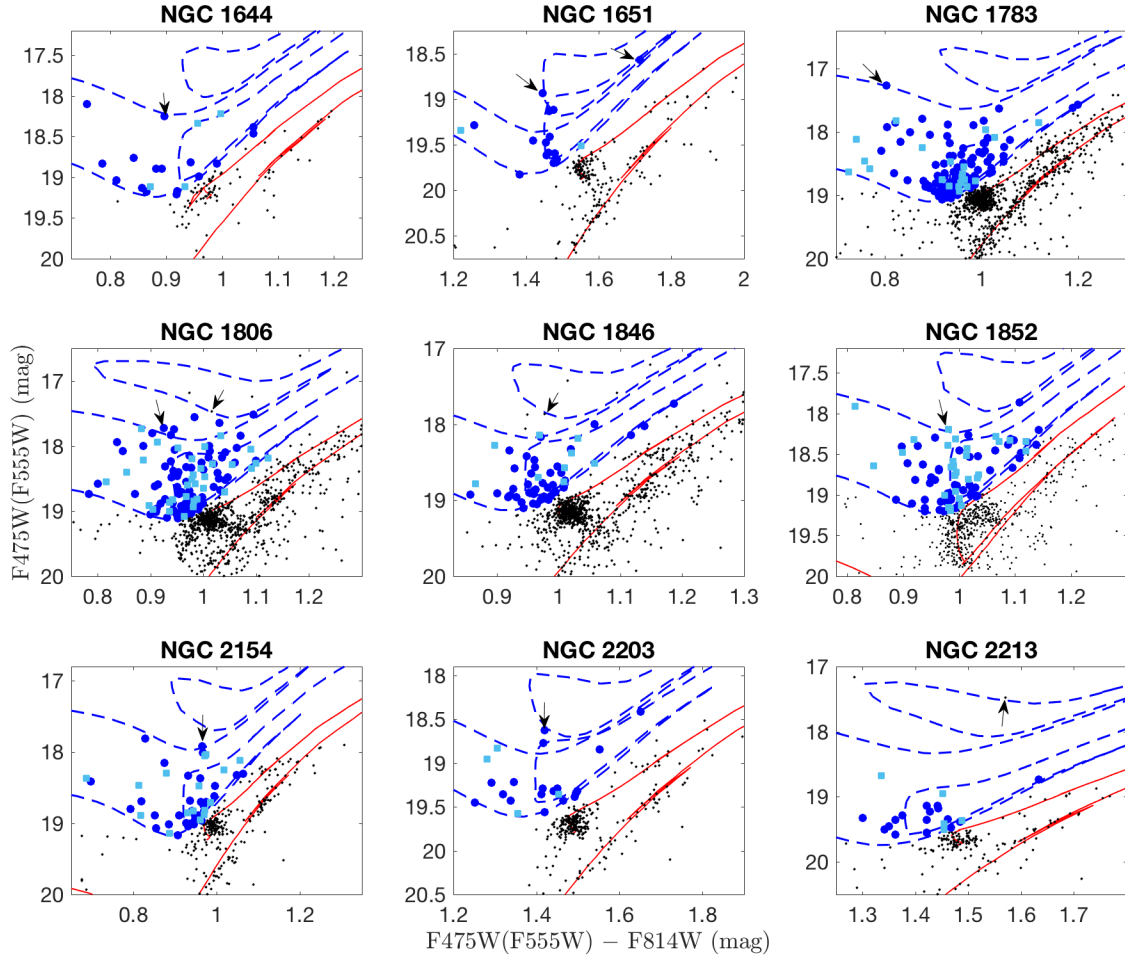


Figure 3. CMDs of our clusters, zoomed into the RC regions. All eBSS candidates observed in the cluster regions are indicated by dark blue circles, while field-star contaminants are shown as light blue squares. The red solid lines are the best-fitting isochrones for the bulk stellar populations. Blue solid lines are the adopted young isochrones which roughly define the magnitude boundaries for selecting the eBSSs. Arrows indicate stars that were used to determine the top boundaries (through visual inspection).

DOLPHOT2.0. Finally, we removed those artificial stars that would be saturated in the observed reference fields. For this reason, there are some very bright evolved stars in some panels of Fig. 3 that were not selected for further analysis (but they were used to determine the youngest isochrones used for the fitting boundaries).

However, simply using isochrones to define bright evolved stars is not reliable. Because real observations always contain scatter and field contamination, we must examine if these bright evolved stars are simply caused by effects of photometric artifacts or by field contamination.

3.1. Photometric Scatter, Distance Spread, and Differential Reddening

In real observations, numerous photometric effects may introduce scatter: (a) Photometric uncertainties will broaden evolutionary patterns (i.e., RGB, RC, and AGB) for normal evolved stars. Very large photometric uncertainties may scatter normal stars into the adopted region for bright evolved stars, erroneously making us treat them as massive stars. (b) Stars may occasionally blend with other stars or with their diffraction patterns, with extended sources (such as background galaxies), cosmic rays, and/or bad pixels. These crowding effects will change the positions of stars in their CMD.

The distances to stars in a star cluster are not exactly identical. In a star cluster, stars at slightly different distances will produce a vertical structure across the RC in their CMD (Girardi 2016). For example, if we assume

Table 3. Best-fitting parameters of the adopted isochrones

Cluster	$\log t_1$	$\log t_2$	$\log t_3$	$\log t_{2M_1}$	M_1	M_2	M_3	$M_3/(2M_1)$	Z^*	A_V	$(m - M)_0$
	[yr]	[yr]	[yr]	[yr]	(M_\odot)	(M_\odot)	(M_\odot)			(mag)	(mag)
	(1)	(2)	(3)	(4)	(5)	(6)	(7)	(8)	(9)	(10)	(11)
NGC 1644	9.20	8.85	8.57	8.40	1.70	2.27	2.90	85.29%	0.008	0.03±0.02	18.50
NGC 1651	9.26	8.83	8.70	8.45	1.59	2.27	2.54	79.87%	0.006	0.31±0.02	18.50
NGC 1783	9.23	8.80	8.40	8.43	1.62	2.32	3.33	102.78%	0.006	0.06±0.02	18.50
NGC 1806	9.25	8.80	8.47	8.45	1.55	2.26	3.05	98.39%	0.004	0.24±0.04	18.50
NGC 1846	9.22	8.80	8.54	8.42	1.64	2.32	2.93	89.33%	0.006	0.15±0.03	18.50
NGC 1852	9.10	8.80	8.53	8.31	1.80	2.32	2.99	83.06%	0.006	0.24±0.03	18.50
NGC 2154	9.21	8.83	8.50	8.41	1.65	2.27	3.04	92.12%	0.006	0.09±0.02	18.50
NGC 2203	9.22	8.80	8.60	8.42	1.64	2.32	2.78	84.76%	0.006	0.22±0.02	18.50
NGC 2213	9.25	8.85	8.45	8.44	1.60	2.23	3.18	99.38%	0.006	0.19±0.03	18.50

(1) Age of the bulk population stars (in logarithmic units). (2, 3) Upper, lower limits to the ages of the young evolved stars. (4) Age of the population with twice the mass of the bulk stellar population. (5) Mass of bottom RGB star of the bulk population. (6, 7) Lower, upper limits to the masses of the bright evolved stars. (8) Mass ratio of the upper mass limits to twice the mass for the bottom RGB star. (9) Metallicity. (10) Reddening and internal spread (differential reddening). (11) Distance modulus. *: $Z_\odot = 0.0152$

that most stars in NGC 1783 are located at its tidal radius (~ 180 pc; see Table 2), at the distance of the LMC (50 kpc) this will produce a magnitude spread of up to ~ 0.016 mag in each passband³.

A cluster region may contain many dusty clumps, which will produce an inhomogeneous reddening distribution across the whole cluster region. The differential reddening may scatter normal stars into the regions of bright evolved stars as well. The typical reddening spread for many old GGCs is $\Delta E(B - V) \sim -0.04$ to 0.04 mag (Milone et al. 2012). Differential reddening for Magellanic Cloud clusters is not well-studied. Martocchia et al. (2017) investigated the differential reddening level in the region of NGC 419, a Small Magellanic Cloud (SMC) cluster with a similar age as our sample clusters. They concluded that the reddening in the F336W filter (A_{F336W}) does not exceed 0.02 mag, which roughly corresponds to a maximum reddening spread of $\Delta E(B - V) = 0.004$ mag. However, Zhang et al. (2018) studied the extinction map for the cluster region of NGC 1783 using the same method as Milone et al. (2012), concluding that the maximum extinction variation across the cluster region ranges from $\Delta E(B - V) \sim -0.03$ to 0.06 mag.

Effects (a) and (b) can be studied through artificial star (AS) tests. The principle underlying AS tests is to generate a sample of fake stars using the same point-

spread-function (PSF) as for the real stars⁴, and then input these fake stars into the raw image and recover them using the same method as applied to the real stars.

The effects of differential reddening can be explored by examining the shape of the RC. A dusty cluster will exhibit an elongated RC (as well as other elongated features) along the reddening direction. Comparing mock observations produced based on AS tests, which only included broadening by photometric artifacts, to real observations helped us quantify the possible level of any differential reddening.

To study the combination of these effects, for each cluster we simulated a population of normal evolved stars. We generated these simulated stellar populations following four steps:

1. Generate a sample of ASs with a Kroupa-like mass function (Kroupa 2001). All ASs are initially located on the best-fitting isochrone. In order to derive a statistically robust result for estimating the effect of photometric scatter, the total number of ASs is more than 20 times that of the observations.
2. Assume a Gaussian distribution of distances for all stars between $d - r_t$ and $d + r_t$, where d is the central distance to the cluster and r_t is its best-fitting tidal radius. Then correct individual stars for the differences in distance modulus.

³ $\Delta M = 5 \log 50180 - 5 \log 49820$

⁴ Because space observations are not affected by atmospheric seeing, HST PSFs for individual stars only depend on their (known) position on the CCD.

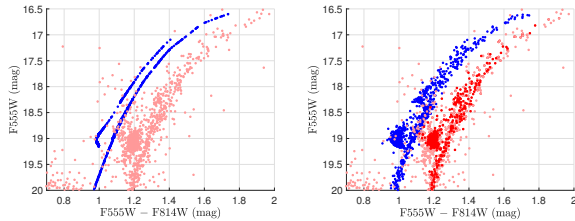


Figure 4. Comparison of a simulated, evolved stellar population with the real observations of NGC 1783. Blue and red dots represent simulated and observed stars, respectively. The observed CMD has been shifted by 0.2 mag in color. The left-hand panel shows input ASs not affected by any scatter; the right-hand panel shows the output artificial stars, which are affected by photometric artifacts, a distance spread, and differential reddening. Dark red dots represent successfully modeled stars.

3. Input all ASs into the raw image and recover them using the same method as applied to the real observations. We repeated this process many times to avoid blending between two ASs; each time we only input 100 ASs into the raw image.
4. For each star, we randomly assigned an extinction variation, derived from a Gaussian distribution of $\Delta E(B - V)$. We then corrected their magnitudes in each passband using the Cardelli et al. (1989) extinction curve with $R_V = 3.1$. $\Delta E(B - V)$ was determined by comparing the resulting mock CMDs to real observations.

In Fig. 4 we show a comparison of the simulated, evolved stellar population with the real observations of NGC 1783. The main features of the RGB, AGB, and RC of NGC 1783 are well reproduced by our simulation. The derived differential reddening levels for our sample clusters are indicated by the reddening uncertainties in Table 3.

We then directly compared the observed CMDs with our simulations. Here we simply wanted to examine if all these effects will scatter many normal evolved stars into the region occupied by the bright evolved stars. In Fig. 5 we show the CMDs of both the selected bright evolved stars and the simulated normal stars for our clusters.

As shown in Fig. 5, a small fraction of stars indeed scatter into the region of the bright evolved stars. We found that most of these scattered stars are RC stars. To further quantify the combined effects of photometric artifacts and any internal distance and reddening spreads, we calculated the number ratio of ASs that were scattered into the eBSS region to all artificial evolved stars, which we call the scatter probability. Next, we estimated the number of normal evolved stars whose distances and reddening properties can be adequately modeled by our

artificial stellar populations. To do this, we evaluated the distance between all observed stars and their nearest AS in the CMD. For each observed star, if we could find an AS within the 3σ photometric uncertainty, we treated it as a successfully modeled star. The number difference of successfully modeled stars between the cluster region and the reference field defines the expected number of normal evolved stars in the star cluster. These numbers multiplied by the scatter probabilities determine the expected numbers of scattered stars in the real observations, which are listed in Table 4. Our results show that the expected number of stars that are scattered into the eBSS region varies from less than one (NGC 1644, NGC 1651, and NGC 2154) to 15 (NGC 1852). However, these numbers are all significantly smaller than the observed numbers of bright evolved stars in our clusters. In addition, the color–magnitude distributions of these contaminating stars are centered close to the RC. In contrast, the observed bright evolved stars are more dispersed, with many of them found close to the upper boundary. We therefore conclude that the populations of observed bright evolved stars cannot be fully explained by the scatter of measurement.

3.2. Field Contamination

Because the LMC is a star-forming galaxy, its field population contains many young stars that may contaminate our observed clusters. However, because of the large distance to the LMC and the crowded environments of its star clusters, direct examination if an individual star observed in any of our clusters is a member star (based on proper motion or radial velocity analysis) is not possible. A frequently used method is to compare the cluster’s CMD to the CMD of its nearby field. If the number of observed bright evolved stars in the cluster region is significantly larger than that in the reference field (per unit area), the normalized number difference should be statistically equal to the number of genuine cluster members. In Table 4 we present the observed numbers of bright evolved stars in the cluster regions (N_{cl}) and the reference fields (N_f), as well as the expected number of field contaminants in the cluster regions (N_{con}) after correcting for the difference in observational area. We list the area ratio of the reference field and the cluster region as well.

We find that for all our clusters, the observed numbers of bright evolved stars in the cluster regions are at least twice those in the reference fields (except for NGC 1852). These differences are statistically significant, which proves that for our clusters, at least $\sim 50\%$ of the observed eBSS candidates are likely genuine cluster members.

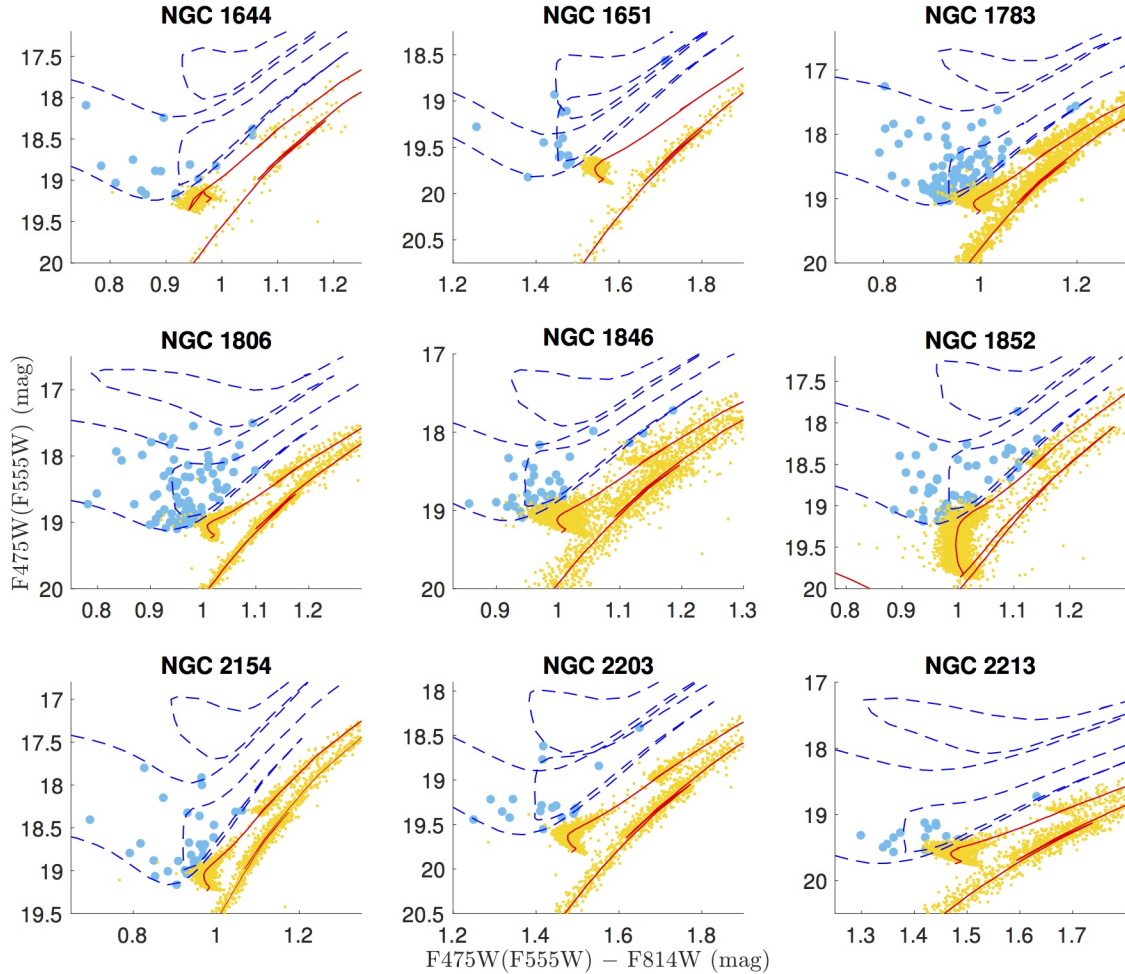


Figure 5. CMDs of the bright evolved stars (blue circles) as well as the simulated normal evolved stars (orange dots). The blue and red solid lines are isochrones adopted for fitting the normal population stars and to define the boundaries of the bright evolved-star regions, respectively.

To further verify the cluster membership probabilities of the observed bright evolved stars, a promising approach is to check their spatial distributions. Because field stars are not gravitationally bound to the cluster, their spatial distribution should be roughly homogeneous. Genuine populations of cluster member stars should exhibit a clear central concentration.

We present the spatial distributions of all selected bright evolved stars and their field counterparts in Figs 6–14 (left-hand panels). As shown in the right-hand panels of these figures, all observed bright evolved stars are apparently concentrated toward the cluster center. The spatial distributions of these bright evolved stars are smoking guns, proving that most of these bright evolved stars are cluster members rather than field stars.

We applied a Monte Carlo-based method to statistically quantify the probability that the observed central concentrations of bright evolved stars are simply derived from the underlying fields. To do so, for each cluster we first calculated the observed central concentrations at different radii. At a given radius R , the corresponding concentration is defined as the number ratio of the stars within this radius and all stars in the cluster region, $c = N(\leq R)/N_{\text{tot}}$. Then we randomly generated N' field stars which were homogeneously distributed in the cluster region, where N' was derived from a Gaussian distribution centered at N_{cont} (Table 4) with a Poisson-like uncertainty. Then, for these N' field stars, we calculated their corresponding concentration at radius R , $c' = N'(\leq R)/N'$. We repeated this procedure 10,000 times for each radius and counted how many times we

Table 4. Expected numbers of scattered stars in the real observations. Following the cluster name (1), the first data block lists the observed number of bright evolved stars in the cluster (2) and in the reference field (3), the expected number of contaminating field stars (4), and the area ratio of the reference field to the cluster region (5). The second data block contains the number of modeled giant stars (6), the expected number of scattered stars (7), and the scatter probability (8).

Cluster (1)	N_{cl} (2)	N_{f} (3)	N_{cont} (4)	$A_{\text{f}}/A_{\text{c}}$ (5)	N_{giant} (6)	N_{scat} (7)	P_{sca} (8)
NGC 1644	17	4	~ 5	0.79	~ 41	< 1	0.56%
NGC 1651	15	4	2–3	1.55	~ 113	< 1	0.40%
NGC 1783	100	23	23	1	919	~ 6	0.70%
NGC 1806	86	34	34	1	565	~ 2	0.40%
NGC 1846	43	9	13–14	0.65	784–785	~ 12	1.50%
NGC 1852	56	30	30	1	394	~ 13	3.35%
NGC 2154	33	16	16	1	205	1–2	0.73%
NGC 2203	18	8	5–6	1.55	218–219	< 1	0.07%
NGC 2213	16	8	5–6	1.55	~ 92	4–5	4.93%

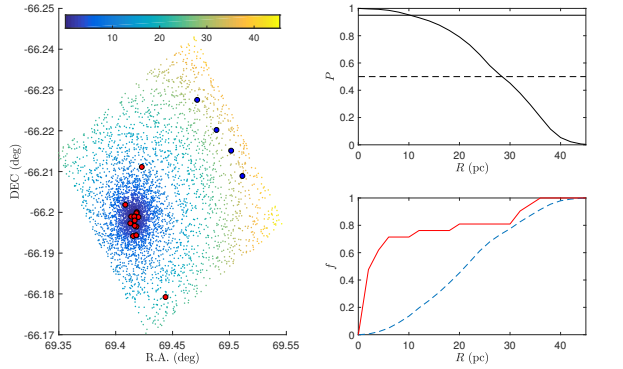


Figure 6. (left) Spatial distributions of all stars in NGC 1644, the selected bright evolved stars (red circles), and their corresponding field contaminants (blue circles). The colors of the background points indicate their 2D distance to the cluster center. (top right) Probability that stars inside different radii are produced by genuine cluster stars. The solid and dashed horizontal lines indicate significance levels of 95% and 50%, respectively. (bottom right) Cumulative profiles of the observed bright evolved stars (red solid lines) and simulated field stars (blue dashed lines).

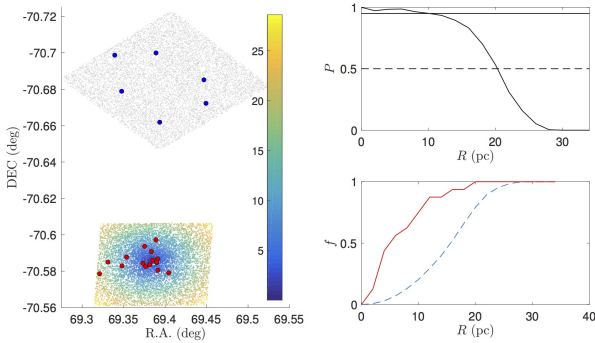


Figure 7. As Fig. 6 but for NGC 1651.

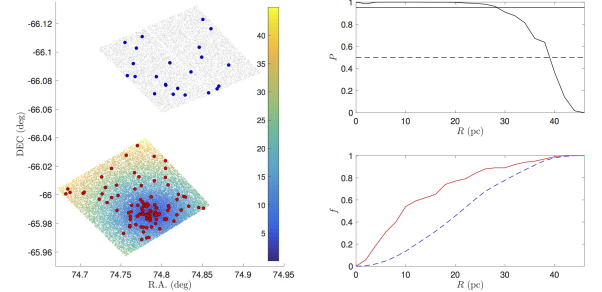


Figure 8. As Fig. 6 but for NGC 1783.

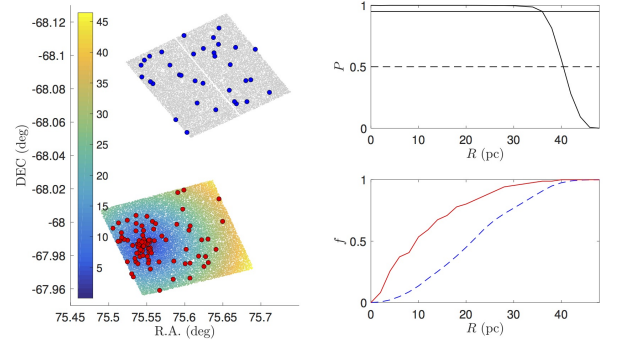


Figure 9. As Fig. 6 but for NGC 1806.

derived $c \leq c'$. This number, divided by 10,000, was defined as the cluster membership probability for stars inside this radius, $P = P(R)$. These cluster membership probabilities, as a function of radius from the cluster center, are presented in the top right-hand panels of Figs 6–14. Using the simulated field stars, we also calculated their cumulative profiles. These field cumulative profiles were used for comparison with those of the ob-

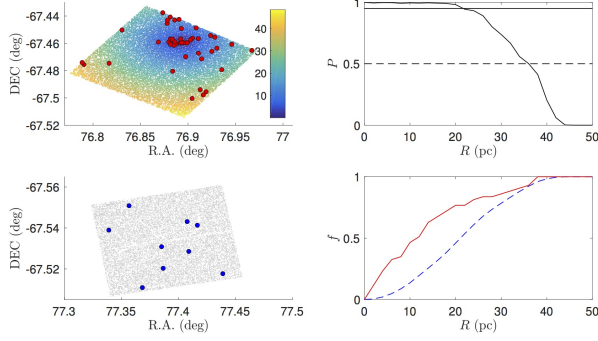


Figure 10. As Fig. 6 but for NGC 1846.

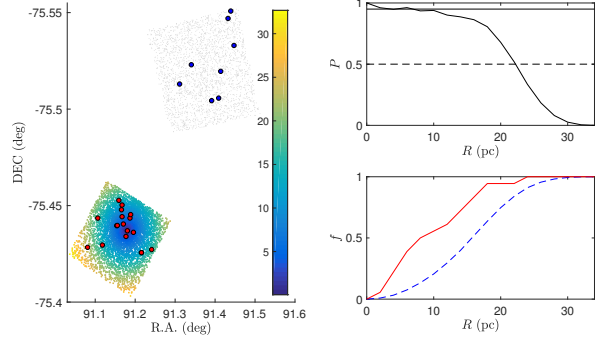


Figure 13. As Fig. 6 but for NGC 2203.

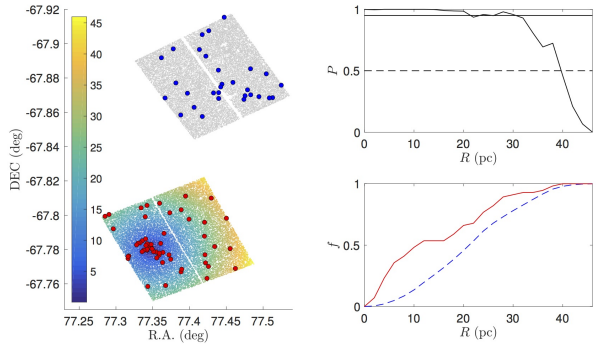


Figure 11. As Fig. 6 but for NGC 1852.

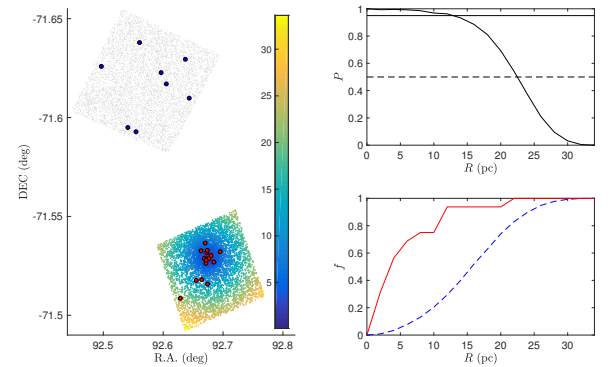


Figure 14. As Fig. 6 but for NGC 2213.

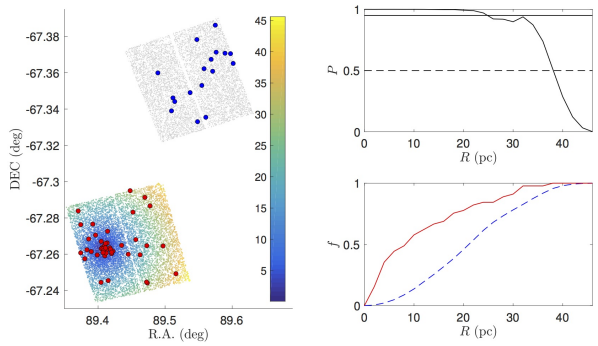


Figure 12. As Fig. 6 but for NGC 2154.

served bright evolved stars. These results are presented in the bottom right-hand panels of Figs 6–14.

Figures 6–14 have proved that field stars cannot realistically reproduce highly concentrated spatial distributions such as those of the observed bright evolved stars. If the observed concentrations of bright evolved stars are simply produced by homogeneously distributed field stars, our calculated cluster membership probabilities should be $\leq 50\%$ for all radii. In the top right-hand panels of Figs 6–14, we have highlighted probability levels of 50% (black dashed lines) and 95% (black solid

lines). The latter indicates a strong concentration level. Clearly, for most of our clusters the observed concentration levels are significantly higher than what could be produced by field stars. This is also illustrated by the difference between the cumulative profiles of the observed eBSS candidates and the simulated field stars.

In summary, because (1) the numbers of field stars are significantly lower than those of the observed bright evolved stars in the cluster regions, and (2) the observed bright evolved stars are all spatially concentrated in the central cluster regions, we conclude that most detected bright evolved stars are most likely genuine cluster members rather than field stars.

4. PHYSICAL IMPLICATIONS

We first examine if these bright evolved stars could be mimicked by a spread in their chemical abundances. In principle, spreads in the overall metallicity, helium, and α -element abundances could cause spreads in both color and luminosity for a single-aged population of stars. Increasing the metallicity contributes to the prevailing stellar opacity, which would lead to an increase of the cooling efficiency. An enhanced metallicity would thus decrease the stellar surface temperature. In the mean-

time, the enhanced opacity would prevent the central energy from radiating to the stellar surface, making a metallicity-enhanced star look fainter than its lower-metallicity counterparts. Therefore, to reproduce an evolved stellar population (for a fixed age) that is obviously brighter and bluer than the normal giant stars, the stars must have a much lower metallicity. However, we found that for each of our clusters, even if we decreased their metallicity to $Z = 0.001$ (which corresponds to almost 6% of solar metallicity; note that all of our clusters have roughly half-solar metallicity, based on isochrone fitting), we could not reproduce the full set of observed bright evolved stars. In addition, such a large metallicity spread would produce a secondary MS that is bluer than the zero-age MS (ZAMS), which is not observed in our sample clusters. In the left-hand panel of Fig. 15, we take the cluster NGC 1783 as an example. The adopted metallicities for the four isochrones are $Z = 0.006, 0.004, 0.002, 0.001$.

Another possible effect that might cause a spread of a single-aged stellar population in the CMD is related to the presence of a helium spread. Unlike metallicity differences, enhanced helium abundances would decrease the stellar radiative opacity, because the average opacity of helium is lower than that of hydrogen. On the other hand, an increased helium mass fraction would lead to a decrease of the hydrogen mass fraction, which would increase the mean molecular weight, thus leading to a stellar luminosity increase. The combination of these effects would make a helium-enhanced star hotter and brighter at each stage than its normal counterpart. However, such increased luminosities (and thus the hydrogen-burning efficiency) would shorten the stellar MS lifetimes. Therefore, a coeval stellar population containing different helium abundances would have a hotter and brighter MS and RGB, but a fainter MSTO and SGB.

To produce a population of brighter evolved stars with the same age as the normal stars, we have to increase their helium abundance. Because the helium abundance is not a free parameter in the PARSEC models, we used the Dartmouth stellar evolution database to generate a sample of isochrones with different helium abundances (Dotter et al. 2007, 2008)⁵. The Dartmouth models offer three choices for the helium abundance, $Y = 0.245 + 1.5Z$, 0.33, and 0.4. For all our clusters, the first choice we adopted was $Y = 0.251, 0.254, 0.257$, corresponding to $Z = 0.004, 0.006, 0.008$, respectively. However, the Dartmouth models do not include post-

RGB phases in their isochrones. We therefore simply shifted the RGB to fit the AGB and the RC, since the AGB is roughly parallel to the RGB. This may lead to some additional uncertainties, but it should not significantly change our results, because an enhanced helium abundance should have the same effect on both RGB and AGB stars. Finally we confirm that even if we enhance the helium abundance to $Y = 0.4$, this is still too small to reproduce the observed bright evolved stars. In addition, this will produce a broadened SGB in all clusters, while some of these clusters exhibit very tight SGBs instead (e.g., Li et al. 2014; Bastian & Niederhofer 2015). We thus exclude the possibility that the observed bright evolved stars are helium-enhanced stars. In the middle panel of Fig. 15 we show isochrones defined by different helium abundances for NGC 1783 as an example.

The impact of enhanced α elements to isochrones has been studied by Salaris et al. (1993). The contribution of α -element enhancements can be taken into account by simply rescaling standard models to the global metallicity, $[M/H]$:

$$[M/H] = [Fe/H] + \log(0.638f_\alpha + 0.362), \quad (2)$$

where f_α is the enhancement factor pertaining to the α elements, $f_\alpha = 10^{[\alpha/Fe]}$. For the solar α abundance $[\alpha/Fe] = 0$, this relation obviously yields $[M/H] = [Fe/H]$. Therefore, the effect of a spread in α elements is similar to that of a metallicity spread. To produce a population of brighter evolved stars, we need to decrease the α abundances. Again, we employed a sample of isochrones with different α -element abundances, down to $[\alpha/Fe] = -0.2$ ⁶, but with fixed $[Fe/H]$, Y , and age. We found that the effect of an α -element spread is negligible compared to the color spread of these bright evolved stars (see the right-hand panel of Fig. 15 for NGC 1783 as an example).

In summary, we have not found any evidence to suggest that these bright evolved stars can be fully reproduced by an internal chemical spread. The only viable explanation is that they are much younger than the clusters' bulk population stars. Here the question is whether they are genuine young stars formed through a continuous star-formation process or if they have a dynamical origin, e.g., as for BSSs.

All our clusters harbor extended MSTO (eMSTO) regions (e.g., Milone et al. 2009). Initially, the most straightforward explanation for the eMSTO region of individual clusters was thought that these clusters could

⁵ <http://stellar.dartmouth.edu/models/index.html>

⁶ The minimum value in the Dartmouth stellar evolution database.

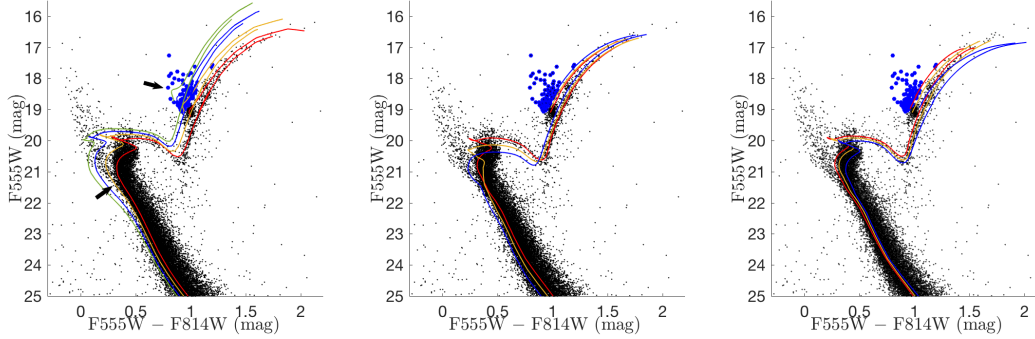


Figure 15. Isochrone fitting for NGC 1783. (left) All isochrones have fixed age but pertain to different metallicities. Red, orange, blue, and green isochrones correspond to $Z = 0.006, 0.004, 0.002, 0.001$, respectively. (middle) All isochrones have fixed age and metallicity but different helium abundances. Red, orange, and blue isochrones indicate $Y = 0.254, 0.33, 0.4$, respectively. (right) All isochrones have fixed age, metallicity, and helium abundance, but have different α -element abundances, $[\alpha/\text{Fe}]$. Red, orange, and blue isochrones correspond to $[\alpha/\text{Fe}] = -0.2, 0, 0.2$ dex, respectively.

have experienced an extended star-formation history lasting several hundred million years (e.g., Goudfrooij et al. 2011, 2014). However, discussions in the literature soon pivoted to an explanation based on the presence of a population of rapidly rotating stars (Bastian & de Mink 2009; Brandt & Huang 2015), because the extended star formation history scenario suffers from many difficulties when dealing with details in other CMD regions (Li et al. 2014, 2016) and when considering global features pertaining to the inferred age spread and the isochronal age of the clusters (Niederhofer et al. 2015). However, some recent studies have suggested that some clusters may still require a genuine age spread to reproduce their very wide MSTO regions Goudfrooij et al. (2017); Piatti & Cole (2017). This discussion continues unabated.

If the scenario proposed by Goudfrooij et al. (2011) is on the right track, this may indicate that the observed bright evolved stars in our clusters are genuine stars formed through a continuous star-forming process. However, all of the bright evolved stars are located beyond an isochrone that is at least 600 Myr younger than the bulk population stars (see Table 3), where Goudfrooij et al. (2011) have determined that the star-formation histories of star clusters such as those observed in the Magellanic Clouds can only last for up to ~ 500 Myr. Therefore, an extended period of star formation seems unable to explain these observed bright evolved stars. In particular, if the presence of these very bright stars would indicate an even longer star-formation history in these clusters, we would expect to see some pre-main-sequence (PMS) stars with ages of 200–500 Myr. Such PMS stars may exhibit an $H\alpha$ excess, which can be easily detected in the *HST* UVIS/WFC3 F656N passband. Such a survey has recently been carried out by Milone et al. (2018), aiming to search for Be stars

in young LMC clusters. No obvious PMS features were detected in their clusters, which thus indirectly supports the notion that the star-forming process in many LMC clusters cannot last so long.

Mergers of two clusters with different ages (Hong et al. 2017), or of a cluster and a giant molecular cloud (GMC; Bekki & Mackey 2009), may produce a stellar system composed of multiply aged stellar populations. LMC and SMC systems may have experienced close encounters some 100 Myr and 1–2 Gyr ago (Gardiner & Noguchi 1996). If such an LMC–SMC tidal interaction would trigger frequent interactions between clusters or between clusters and GMCs, this may produce large numbers of multiply aged stellar population systems exhibiting similar age differences. However, this scenario cannot explain why the bright evolved stars in our clusters all represent a small number fraction compared with the bulk population stars, since a merger event can involve two stellar systems with various mass ratios.

The most straightforward explanation is that these bright evolved stars are eBSSs. Since the mass limit for BSSs is twice the mass of MSTO stars, their evolved counterparts must have the same mass limit as well. The upper mass limit for our young evolved stars is simply defined by the adopted youngest isochrone. We use the mass of the bottom of the RGB of the youngest isochrone as the typical maximum mass of our young evolved stars. Correspondingly, the mass of the bottom of the RGB of the old isochrone is the typical mass of normal evolved stars. We then check if the former mass would be higher than twice the latter. In Table 3, we list the masses for the bottom of the RGB corresponding to the bulk population and to two young isochrones (columns 5–7), and the mass ratio of the upper mass limit to twice the mass for the bottom of the RGB of the bulk stellar population (column 8). We also list the

age for a stellar population with exactly twice the mass for the bulk population stars. We found that, except for NGC 1783, all clusters should have bright evolved stars that are less massive than twice the mass of their normal evolved counterparts. It is likely that these observed bright evolved stars are eBSSs formed through interactions between first-generation stars. For NGC 1783, there is only one star slightly more massive than twice the mass of the normal evolved stars, as indicated by the arrow in Fig. 3. Given that NGC 1783 contains the largest sample of eBSS candidates (100), one exception may simply be caused by fitting uncertainties and does not change our conclusions.

We found that all of our clusters would have bright evolved stars that are less massive than twice the mass of their normal evolved counterparts. It is likely that these observed bright evolved stars are eBSSs formed through interactions between first-generation stars.

To further explore their origin, we calculated the collisional rate for the core regions of our clusters (Davies et al. 2004),

$$N_{\text{col}} = 0.03225 \frac{f_{\text{mms}}^2 N_c n_{c,5} r_{\text{col}} m_{\text{BSS}}}{V_{\text{rel}}}, \quad (3)$$

where N_{col} represents the number of expected collisional BSSs that would be produced over the last 1 Gyr, f_{mms} is the fraction of massive MS stars in the core region (where ‘massive MS star’ means they are sufficiently massive to form a collisional BSS), and $f_{\text{mms}} = 0.25$ is commonly adopted (Davies et al. 2004). N_c is the number of stars located in the core region. We evaluated this number as follows. We counted the number for MS stars with absolute F814W magnitudes of $\sim 2\text{--}3$ mag (equal to a stellar mass of $\sim 1.2\text{--}1.5 M_{\odot}$). We assumed that these stars follow a Kroupa-like mass function. Then, we evaluated the total number of stars by extrapolating this mass function down to $0.08 M_{\odot}$. We selected stars in this magnitude range, because they will have a high completeness and follow a simple mass–luminosity relationship. $n_{c,5}$ is the stellar number density for the core region in units of 10^5 pc^{-3} , which is the ratio of the number of stars contained in the core region and the core volume. r_{col} represents the minimum separation of two colliding stars in units of the solar radius, R_{\odot} . We assume that it is twice the stellar radius of the BSSs. We assume that the average mass of BSSs is equal to that of our observed young evolved stars, as indicated by the best-fitting isochrones. Their radii were evaluated through the empirical formula introduced by (Demircan & Kahraman 1991). V_{rel} is the relative incoming velocity of binaries,

$$V_{\text{rel}} = \sqrt{2}\sigma = \sqrt{\frac{4GM_c}{r_c}}, \quad (4)$$

where σ is the velocity dispersion for all stars in the core region. M_c is the stellar mass of the cluster core, since we have already evaluated the total number of stars in the core region following a Kroupa mass function, M_c is simply the sum of the masses of these stars. However, it is possible that we have overestimated the number of stars in the core, since numerous low-mass stars must have evaporated from the central cluster region owing to two-body interactions (e.g., de Grijs et al. 2002).

The resulting stellar collisional rate (N_{col} , per Gyr), as well as the derived global parameters (N_c , $n_{c,5}$, σ , M_c) for our clusters, are summarized in Table 5.

Our calculation shows that it is unlikely that these clusters could produce sufficient numbers of collisional BSSs at their relevant ages, at least for single–single collisional BSSs. However, binary-mediated stellar collisions may dominate the formation of collisional BSSs. Chatterjee et al. (2013) modeled 128 GGCs with various properties to investigate the dominant formation channels of BSSs in these clusters. They find that for central stellar mass density higher than $\sim 10^3 M_{\odot} \text{ pc}^{-3}$, binary-mediated stellar collisions will make a major contribution for BSS formation. In Table 5 we have also listed the mass densities in the core regions of our clusters,

$$\rho_c = \frac{3M_c}{4\pi r_c^3} \quad (5)$$

As we can see, even the densest cluster, NGC 1644, does not have a core density that reaches the density threshold of $\sim 10^3 M_{\odot} \text{ pc}^{-3}$. Therefore, binary-mediated stellar collisions are also unlikely major formation channels for these eBSSs in our clusters. If these young evolved stars are eBSSs, they are therefore all most likely produced through binary interactions.

It is also possible that some of these bright evolved stars are not massive stars, but that they are instead unresolved binary systems, which may appear brighter than single stars in the CMD. To explore this possibility, for each cluster, we calculated the loci of the binary sequences for different mass ratios, $q = M_2/M_1$. Here, M_1 and M_2 are masses of the primary and secondary components, respectively. The loci of these binary sequences are calculated as follows.

- i. We selected the best-fitting isochrone to the bulk population as our baseline.
- ii. For each point of the baseline, we calculated the secondary star’s mass for a fixed mass ratio ($M_2 = qM_1$).
- iii. Calculate the magnitude in each passband for the secondary star through interpolation, based on the selected isochrone.

Table 5. Derived physical parameters.

Cluster	N_c	$n_{c,5}$ (10^5 pc^{-3})	σ (km s^{-1})	M_c (M_\odot)	N_{coll}	ρ ($M_\odot \text{ pc}^{-3}$)
	(1)	(2)	(3)	(4)	(5)	(6)
NGC 1644	4.02×10^3	0.0078	3.28	1.33×10^3	0.121	282.69
NGC 1651	1.74×10^4	0.0009	3.68	5.64×10^3	0.059	29.10
NGC 1783	6.95×10^4	0.0016	6.53	2.32×10^4	0.293	54.03
NGC 1806	4.82×10^4	0.0030	6.23	1.53×10^4	0.359	93.76
NGC 1846	5.44×10^4	0.0007	5.14	1.78×10^4	0.120	21.67
NGC 1852	1.98×10^4	0.0010	3.98	6.78×10^3	0.076	8.32
NGC 2154	1.41×10^4	0.0019	3.90	4.63×10^3	0.112	62.17
NGC 2203	1.30×10^4	0.0007	3.17	4.24×10^3	0.041	21.34
NGC 2213	3.26×10^3	0.0024	2.48	1.06×10^3	0.056	78.06

(1) Expected number of stars in the core region. (2) Central number density (in units of 10^5 pc^{-3}). (3) Central velocity dispersion. (4) Core mass. (5) Expected number of collisional BSSs formed during the last 1 Gyr.

iv. Calculate the resulting magnitude,

$$m = -2.5 \log(10^{-0.4m_1} + 10^{-0.4m_2}), \quad (6)$$

where m , m_1 , and m_2 are magnitudes of the binary system and its primary and secondary components, respectively.

v. Connect all points for the resulting magnitudes calculated in step (iv), which is the locus of a binary sequence with a mass ratio q .

In Fig. 16, we present the calculated binary sequences, compared with the observed young evolved stars in the CMDs. It is clear that only high mass-ratio binaries (with $q \geq 0.65$ – 0.75) will have their unresolved photometric magnitudes significantly different from the loci of the single stars. This is because our stars are so bright that only a secondary star with comparable luminosity would significantly affect the photometry. The secondary star must be very massive, probably a giant star. This is because compared with a giant star, a low-mass MS component is too faint to affect the photometry. In Fig. 16, the red curves from right to left are binary loci with mass ratios of $q = 0.65$ to 0.95 . These loci are all bluer than the normal RGB because these binaries all contain a secondary star that is bluer than the primary, evolved star. Once the mass ratio reaches unity, $q = 1$, the binary locus moves back to the red side, because in that case all binaries simply contain two equal-mass giant stars. It is parallel to the bulk stellar population but it is -0.752 mag brighter.

As shown in Fig. 16, many bright evolved stars observed in our clusters are located in the region covered by binary sequences for different mass ratios. Therefore, it is possible that the bright evolved stars are not massive stars but unresolved high mass-ratio binary systems. In particular for NGC 1852, almost all of its bright

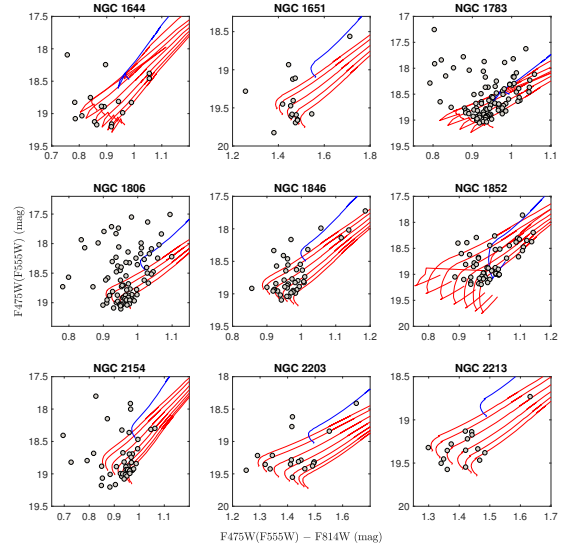


Figure 16. Observed bright evolved stars in our clusters as well as binaries sequences for different mass ratios. The blue solid lines represent the equal-mass binary sequences. The red solid lines are binary sequences for mass ratios of less than one, from bottom to top the mass ratio increases.

evolved stars are located in the region of high mass-ratio binaries. However, unresolved binaries only cover a very small region in the CMD. They are able to explain some stars which are very close to the normal stellar population. To explain stars that are very blue and bright, like those in NGC 1783, NGC 1806, or NGC 2154, a significant population of massive stars is still required.

To separate massive single stars and unresolved binaries, observations in far-ultraviolet (far-UV) passbands would provide useful information, such as in the *HST* UVIS/WFC3 F225W and F275W bands. In the far-UV, the less-evolved stars are even brighter than the more

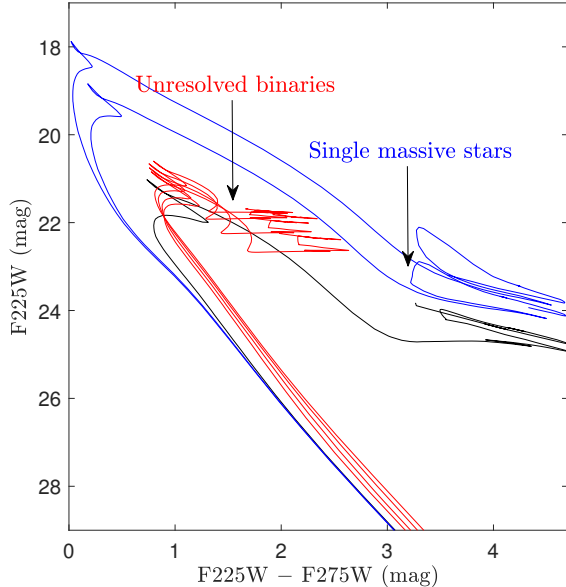


Figure 17. Illustration of how far-UV CMDs (based on the F225W and F275W passbands) could allow us to distinguish unresolved binaries from single massive evolved stars, taking NGC 2203 as an example. The red solid curves represent unresolved binaries with different mass ratios. The blue and black curves are young and old isochrones, respectively, adopted for the cluster. All isochrones were generated by the PARSEC stellar evolution model (Bressan et al. 2012).

evolved stars, since the latter would move to the red. For unresolved binaries composed of two first-generation stars, the total flux of these binary systems might be dominated by the less-evolved components. The resulting photometry for these binary systems will be close to the MS in the CMD. On the other hand, genuine massive evolved stars will appear much redder and brighter than unresolved binaries. In Fig. 17, taking NGC 2203 as an example, we show the adopted young isochrones, as well as the predicted loci of binary sequences with different mass ratios, in the F225W–F275W CMD. The positions of the unresolved binaries and genuine young evolved stars are indeed well separated in the CMD.

In summary, the detected bright evolved stars in our clusters are most likely eBSSs, it is also possible that some are simply unresolved binaries.

If these bright evolved stars are indeed eBSSs, it seems that their numbers are large, even comparable to the numbers of normal BSSs observed in old GCs (e.g., Leigh et al. 2013). However, this does not mean that larger numbers of normal BSSs hide in the MS. Because BSSs are formed through stellar dynamics rather than the collapse of GMCs, it is not necessary that they should form according to a Kroupa-like mass function

(Kroupa 2001). In fact, early-type stars usually have higher binary fractions Duchêne & Kraus (2013), and the overall binary fraction in a dense cluster will continue to decrease over time because of dynamical destruction (Ivanova et al. 2005). Given that most of the progenitors of our eBSSs should be B-type stars, we are not surprised about the large numbers of eBSSs in these clusters. Indeed, Hypki & Giersz (2017) have simulated the number evolution of BSSs in dense clusters for different initial conditions. They found that at ages of 4–5 Gyr, the number of BSSs is expected to reach a peak. For clusters aged 1–2 Gyr, the expected number of BSSs is comparable to that in old GCs (≥ 10 Gyr).

5. CONCLUSION

Based on high-precision multi-band *HST* photometry, we analyzed the CMDs of nine young GCs in the LMC. We found that all these clusters harbor samples of bright evolved stars. After having ruled out the effects of field contamination and photometric artifacts, we conclude that these bright evolved stars are likely genuine cluster members. The main results can be summarized as follows.

- The combination of photometric scatter, internal distance spread, and differential reddening cannot explain the large color–magnitude dispersion of these bright evolved stars. These stars can be well described by isochrones with younger ages, but not by isochrones for different metallicities, helium, or α -element abundances, which means that they are more massive than normal stars, described by an older isochrone.
- Statistical analysis shows that the reference field stars cannot fully explain nor generate these bright evolved stars. Compared with field stars with the same color–magnitude distributions, these bright evolved stars are overdense in the cluster region. In addition, their spatial distributions exhibit clear central concentrations, which cannot be explained by a homogeneous field.
- Unresolved binaries can partially reproduce the color–magnitude distributions of these bright evolved stars. However, such binaries can only cover a very compact region in the CMD. For some stars that are extremely blue and bright, we still require a significant fraction of massive population stars.
- If we assume that all these bright evolved stars are single stars, their masses would not exceed twice the mass of normal evolved stars. We suggest that

this may indicate that most of these bright evolved stars are evolved products of their first-generation stars, that is, they are eBSSs. Our dynamical calculations show that none of our clusters can produce sufficient numbers of collisional BSSs over their lifetimes. Therefore, the only viable explanation for these eBSSs is that they formed through binary interactions.

6. ACKNOWLEDGEMENTS

We thank the anonymous referee for valuable comments. C. L. is supported by the Macquarie Research Fellowship Scheme. This work was supported by the National Key Research and Development Program of

China through grant 2017YFA0402702. L. D. and R. d. G. also acknowledge research support from the National Natural Science Foundation of China (grants U1631102 and 11373010). J. H. acknowledges support from the China Postdoctoral Science Foundation, Grant No. 2017M610694. Parts of this research were conducted with the support of the Australian Research Council Centre of Excellence for All Sky Astrophysics in 3 Dimensions (ASTRO 3D), through project number CE170100013.

Facilities: Hubble Space Telescope (WFC3/UVIS and ACS/WFC)

Software: DOLPHOT2.0 (Dolphin 2016)

REFERENCES

- Andronov, N., Pinsonneault, M. H., & Terndrup, D. M. 2006, *ApJ*, 646, 1160
- Baldwin, A. T., Watkins, L. L., van der Marel, R. P., et al. 2016, *ApJ*, 827, 12
- Bastian, N., & de Mink, S. E. 2009, *MNRAS*, 398, L11
- Bastian, N., & Niederhofer, F. 2015, *MNRAS*, 448, 1863
- Beccari, G., Ferraro, F. R., Lanzoni, B., & Bellazzini, M. 2006, *ApJL*, 652, L121
- Bekki, K., & Mackey, A. D. 2009, *MNRAS*, 394, 124
- Brandt, T. D., & Huang, C. X. 2015, *ApJ*, 807, 25
- Bressan, A., Marigo, P., Girardi, L., et al. 2012, *MNRAS*, 427, 127
- Cardelli, J. A., Clayton, G. C., & Mathis, J. S. 1989, *ApJ*, 345, 245
- Chatterjee, S., Rasio, F. A., Sills, A., & Glebbeek, E. 2013, *ApJ*, 777, 106
- Dalessandro, E., Ferraro, F. R., Massari, D., et al. 2013, *ApJ*, 778, 135
- Davies, M. B., Piotto, G., & de Angeli, F. 2004, *MNRAS*, 349, 129
- Dolphin, A. 2016, *Astrophysics Source Code Library*, ascl:1608.013
- Dotter, A., Chaboyer, B., Jevremović, D., et al. 2007, *AJ*, 134, 376
- Dotter, A., Chaboyer, B., Jevremović, D., et al. 2008, *ApJS*, 178, 89
- Duchêne, G., & Kraus, A. 2013, *ARA&A*, 51, 269
- de Grijs, R., Gilmore, G. F., Johnson, R. A., & Mackey, A. D. 2002, *MNRAS*, 331, 245
- Demircan, O., & Kahraman, G. 1991, *Ap&SS*, 181, 313
- Ferraro, F. R., Paltrinieri, B., Fusi Pecci, F., et al. 1997, *A&A*, 324, 915
- Ferraro, F. R., Beccari, G., Dalessandro, E., et al. 2009, *Nature*, 462, 1028
- Ferraro, F. R., Lapenna, E., Mucciarelli, A., et al. 2016, *ApJ*, 816, 70
- Ferraro, F. R., Lanzoni, B., Dalessandro, E., et al. 2012, *Nature*, 492, 393
- Gardiner, L. T., & Noguchi, M. 1996, *MNRAS*, 278, 191
- Girardi, L. 2016, *ARA&A*, 54, 95
- Goudfrooij, P., Puzia, T. H., Kozhurina-Platais, V., & Chandar, R. 2011, *ApJ*, 737, 3
- Goudfrooij, P., Girardi, L., Kozhurina-Platais, V., et al. 2014, *ApJ*, 797, 35
- Goudfrooij, P., Girardi, L., & Correnti, M. 2017, *ApJ*, 846, 22
- Hills, J. G., & Day, C. A. 1976, *Astrophys. Lett.*, 17, 87
- Hong, J., de Grijs, R., Askar, A., et al. 2017, *MNRAS*, 472, 67
- Hypki, A., & Giersz, M. 2017, *MNRAS*, 466, 320
- Ivanova, N., Belczynski, K., Fregeau, J. M., & Rasio, F. A. 2005, *MNRAS*, 358, 572
- King, I. 1962, *AJ*, 67, 471
- Knigge, C., Leigh, N., & Sills, A. 2009, *Nature*, 457, 288
- Kroupa, P. 2001, *MNRAS*, 322, 231
- Leigh, N., Knigge, C., Sills, A., et al. 2013, *MNRAS*, 428, 897
- Li, C., de Grijs, R., Deng, L., & Liu, X. 2013, *ApJL*, 770, L7
- Li, C., de Grijs, R., Deng, L., 2014, *Nature*, 516, 367
- Li, C., de Grijs, R., Bastian, N., et al. 2016, *MNRAS*, 461, 3212
- Li, C., Deng, L., de Grijs, R., Jiang, D., & Xin, Y. 2018, *ApJ*, 856, 25
- Li, C., & Hong, J. 2018, *MNRAS*, 476, 5274

- Martocchia, S., Bastian, N., Usher, C., et al. 2017, MNRAS, 468, 3150
- McCrea, W. H. 1964, MNRAS, 128, 147
- Milone, A. P., Bedin, L. R., Piotto, G., & Anderson, J. 2009, A&A, 497, 755
- Milone, A. P., Piotto, G., Bedin, L. R., et al. 2012, A&A, 540, A16
- Milone, A. P., Marino, A. F., Di Criscienzo, M., et al. 2018, MNRAS, 477, 2640
- Niederhofer, F., Georgy, C., Bastian, N., & Ekström, S. 2015, MNRAS, 453, 2070
- Niederhofer, F., Bastian, N., Kozhurina-Platais, V., et al. 2016, A&A, 586, A148
- O'Donnell, J. E. 1994, ApJ, 422, 158
- Piatti, A. E., & Cole, A. 2017, MNRAS, 470, L77
- Raso, S., Ferraro, F. R., Dalessandro, E., et al. 2017, ApJ, 839, 64
- Salaris, M., Chieffi, A., & Straniero, O. 1993, ApJ, 414, 580
- Simunovic, M., Puzia, T. H., & Sills, A. 2014, ApJL, 795, L10
- Sun, W., Li, C., de Grijs, R., & Deng, L. 2018, arXiv:1806.04805
- Zhang, H., de Grijs, R., Li, C., & Wu, X. 2018, ApJ, 853, 186